

Detection and analysis of tau neutrino interactions in DONUT Emulsion Target

K. Kodama ^a, G. N. Saoulidou, G. Tzanakos ^b,
B. Baller, B. Lundberg, R. Rameika ^c,
J.S. Song, C.S. Yoon, S.H. Chung ^d, S. Aoki, T. Hara ^e,
C. Erickson, K. Heller, R. Schwienhorst ^f,
J. Sielaff, J. Trammell ^f,
K. Hoshino, H. Jiko, J. Kawada, T. Kawai, M. Komatsu ^g,
H. Matsuoka, M. Miyanishi, M. Nakamura, T. Nakano, K. Narita ^g,
K. Niwa, N. Nonaka, K. Okada, O. Sato, T. Toshito ^g,
V. Paolone ^h, T. Kafka ⁱ

^a*Aichi University of Education, Kariya, Japan*

^b*University of Athens, Greece*

^c*Fermilab, Batavia, Illinois 60510*

^d*Gyeongsang University, Chinju, Korea*

^e*Kobe University, Kobe, Japan*

^f*University of Minnesota, Minnesota*

^g*Nagoya University, Nagoya 464-8602, Japan*

^h*University of Pittsburgh, Pittsburgh, Pennsylvania 15260*

ⁱ*Tufts University, Medford, Massachusetts 02155.*

Abstract

The DONUT experiment used an emulsion/counter hybrid experiment, which succeeded in detecting tau neutrino charged current interactions. A new method of emulsion analysis, NETSCAN, was used to locate neutrino events and detect tau decays. It is based on the fully automated emulsion read-out system (Ultra Track Selector) developed at Nagoya University.

The achieved plate-to-plate alignment accuracy was $\sim 0.2\mu m$ over the area of $2.6mm \times 2.6mm$, permitted an efficient and systematic tau decay search using emulsion data. Moreover, this accuracy allowed the measurement of particle momenta by multiple Coulomb scattering, and contributed to the efficient background rejection for the tau candidates. Details of the methods are described in this paper.

1 Introduction

The first observation of tau neutrino charged current interactions was made by the DONUT experiment. (1). Nuclear emulsion was used as a three-dimensional tracking device with sub-micron accuracy, which enabled the detection of the short-lived τ particle associated with the ν_τ charged current interaction.

The analysis of nuclear emulsion was a time consuming job relying on human scanners until the invention of a semi-automated emulsion scanning system, first used in FNAL/ E531 (2). Though successful results were obtained using this system (3; 4), the analysis speed was limited because it still required some human operation. A prototype of the fully automated system (called Track Selector, TS) appeared in 1984 (5; 6), and was first used in the analysis of the CHORUS experiment (7).

In CHORUS, the analysis was performed by using the first generation TS system in conjunction with predictions from an electronic vertex detector. All of the tracks reconstructed in the vertex detector were scanned and followed to the interaction or decay vertices.

In DONUT, a much faster scanning system and a new offline analysis procedure (called NETSCAN) was required, due to a greater number of background tracks that were recorded during the run. Also, the track reconstruction by the vertex detector was often poor because of electromagnetic showers in the thicker emulsion targets.

Following a description of the DONUT emulsion/fiber-tracker hybrid target, details of the analysis are discussed, emphasizing the methods developed for this experiment.

2 DONUT emulsion-SFT hybrid target

2.1 Structure

The DONUT hybrid target has four emulsion stations interleaved with scintillating-fiber tracking (SFT) stations. A schematic view of the DONUT hybrid target is shown in Fig.1. The thickness of each emulsion target is 7cm corresponding to $2 \sim 3$ radiation lengths depending on the target type as described below. The SFT was used to find the emulsion station in which a neutrino interaction occurred and to predict the vertex position in the emulsion target by detecting the emerging tracks from the interaction.

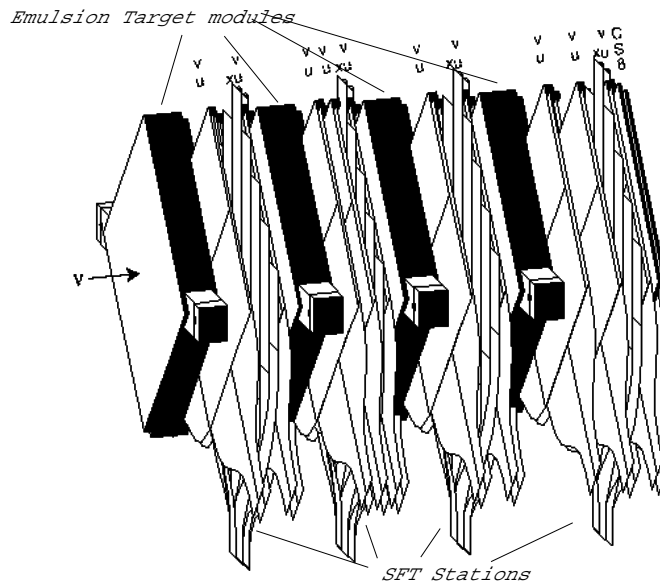


Fig. 1. A schematic view of the DONUT emulsion-SFT hybrid target.

2.2 Emulsion target

There were three distinct emulsion target designs that were exposed in the experiment. All were repeated structures of emulsion sheets stacked perpendicular to the neutrino beam direction. Fig.2 shows the stacking pattern for the three designs. Each design was built from a type of emulsion sheet distinguished by the thickness of the emulsion coating and the supporting plastic, or base layer. The three types of emulsion plates were called ECC(200), ECC(800) and Bulk.

The plate used in ECC(200) had a thin plastic base of $200\mu m$ with a $100\mu m$ coating of emulsion on both sides. ECC(800) had $100\mu m$ emulsion coatings on an $800\mu m$ thick plastic base. The Bulk plates had thick emulsion layers of $350\mu m$ on both sides of a $90\mu m$ thick plastic base. All emulsion plates were $50cm \times 50cm$.

In the two structures named ECC (Emulsion Cloud Chamber), stainless steel plates 1mm thick were interleaved with the emulsion plates in the target assembly. The neutrino interactions predominantly occurred in the steel. The emulsion plates acted effectively as a three-dimensional tracking device. In the bulk type, no steel plates were incorporated, and the emulsion layers act as the neutrino target as in the case of the CHORUS emulsion target.

The emulsion sheets were stacked into sealed target boxes as shown in Fig.3. The plates were kept compressed and fixed under a pressure of $\sim 0.2atm$ created by the evacuation of air in the box. Each target box was made by screwing and glueing two aluminum/honeycomb plates at the upstream and

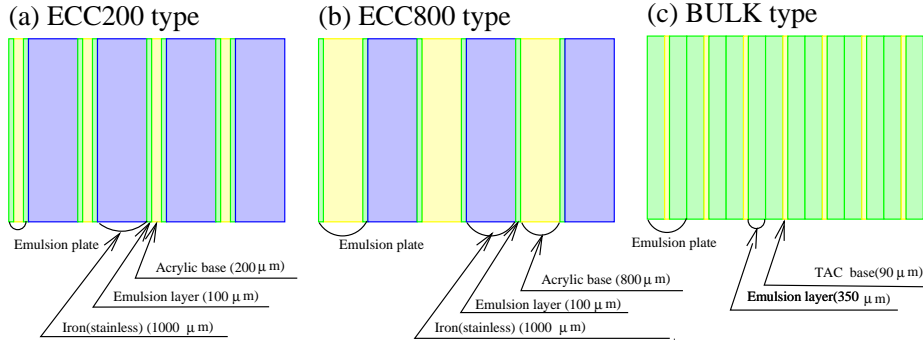


Fig. 2. Structure of the emulsion target with the three basic configurations: (a) ECC(200), (b) ECC(800) and (c) Bulk. Exposed emulsion modules were the combinations of these structures.

downstream ends, 1cm thick, on a 7cm thick aluminum frame. In addition to forming the structure of the target box, the honeycomb plates were designed to hold special emulsion sheets called Changeable Sheets (CS). The CS was a special emulsion sheet used to connect SFT tracks to the emulsion target. The CS were replaced frequently during the run to keep the accumulated track density low compared to the main emulsion target. A grid of collimated x-ray sources on the honeycomb plate formed marks on each exposed CS for spatial calibration.

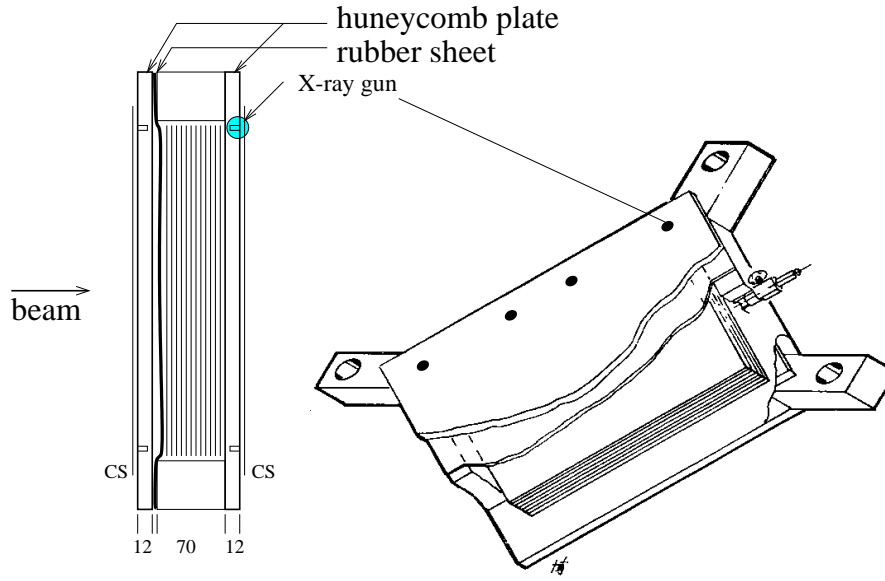


Fig. 3. A schematic view of an emulsion target module. A cross-sectional view is shown to the left.

2.3 Scintillating Fiber Tracker

There were four stations of the SFT as shown in Fig.1. However, in construction, the SFT was composed of only two independent modules. Thus, there were two stations per module as shown Fig.4. The upstream station of each module (indicated as SFT1 in the figure) consists of two U/V doublet planes (the fibers aligned ± 45 degrees with respect to vertical) and one X plane (the fibers aligned vertically) and the downstream station (SFT2 in the figure) has three U/V doublet planes and one X plane as shown in the figure. There was a total of 44 SFT planes in all stations. All planes in each station were mechanically fixed together with an accuracy of $\sim 50\mu m$.

For each U/V doublet plane, two-layered scintillating fiber sheets were glued on both sides of a honeycomb plate (11mm thick). Each X plane consisted of four layers of fibers. The glued positions of the fiber sheets on the plane were measured by an X-Y stage with the accuracy of $10\mu m$. The $500\mu m$ diameter fiber was made from SCSF78 of produced by Kuraray Co. The dopant density was tuned to maximize the light yield at the farthest position ($\sim 120cm$) from the read-out ends. The light yield of the two-layered fiber sheet was about 7 photo-electrons when a *mip* passed through the farthest position. The fiber sheets were produced by machines installed at Nagoya, which were also used for the production of CHORUS fiber trackers (8).

The ends of the fiber sheets were stacked into paddles in contact with the input fiber-optic windows of six Image Intensifier Tubes produced by Hamamatsu Photonics K.K. The images were read-out by CCD cameras and digitized for the triggered events. The hit positions on the CCD images were decoded into fiber coordinates by using maps calibrated by a set of fiducial fibers. The fiducial fibers were flashed for each data run and the positions were monitored for any systematic shifts.

2.4 Alignment between the emulsion target and the SFT

The emulsion modules and the SFT stations were installed on a mechanical support composed of two I-beams holding precision mounting hardware. The design accuracy of the mechanical support was $50\mu m$. The alignment between the emulsion targets and the SFT stations were checked and fine-tuned by using special cosmic ray exposures. For this exposure, seven new CS plates were installed in the CS holders. In the recorded events, tracks with angle smaller than $400mrad$ were selected and scanned on the CS plates. The cosmic ray tracks were reconstructed in the SFT station just upstream of each CS plate, and projected to the CS. The distribution of the residuals between the pro-

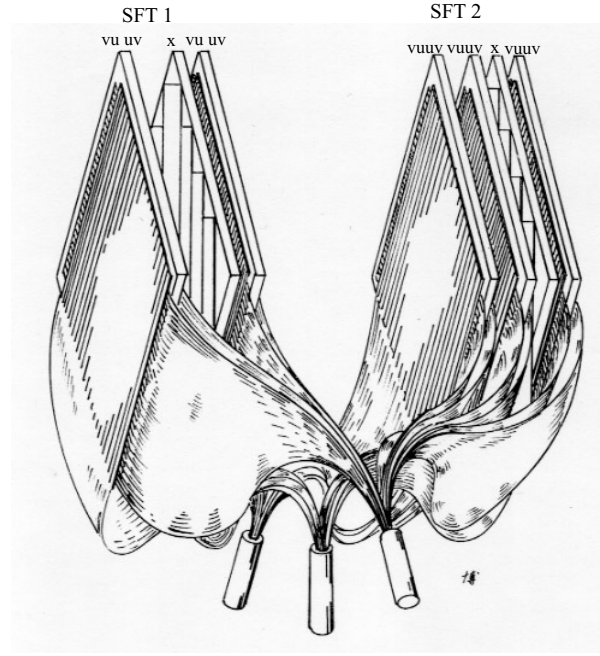
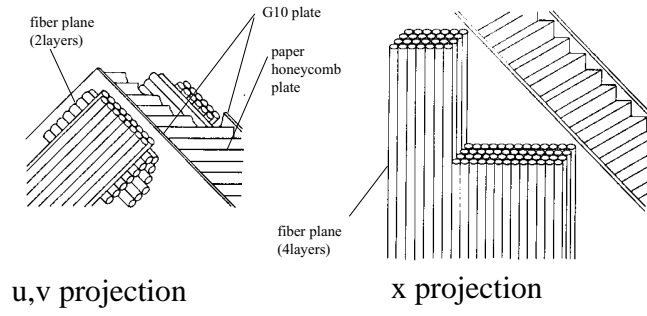


Fig. 4. A schematic view of one SFT module.

jections and the found tracks are shown in Fig.5. The RMS of the distribution is consistent with measurement errors. The mean of the distributions indicate the shift from design within the mechanical accuracy, shown in Fig.6.

3 Beam exposure

A "prompt" neutrino beam was created by interacting 800GeV/c protons in 1m long tungsten beam dump. The neutrino beam that was created had the following approximate composition: 60% ν_μ , 35% ν_e , and 5% ν_τ , with equal numbers of anti-neutrinos and neutrinos. The emulsion target was 36m downstream of the beam dump. In addition to the emulsion targets and SFT, the DONUT detectors consisted of a magnetic spectrometer, electromagnetic

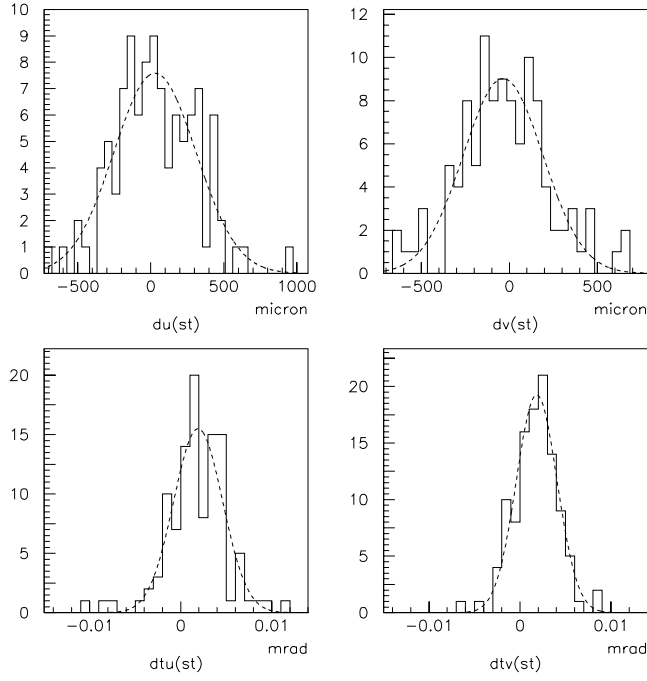


Fig. 5. Residual distributions of position (top figures) and angle (bottom figures) between the predictions and the found tracks for cosmic ray calibration. The rms of the distributions are $280\mu m$ for U, $230\mu m$ for V, $2.7mrad$ for θ_U and $2.2mrad$ for θ_V . The theoretical resolution is $220\mu m$ for U/V and $2.2mrad$ for θ_{proj} .

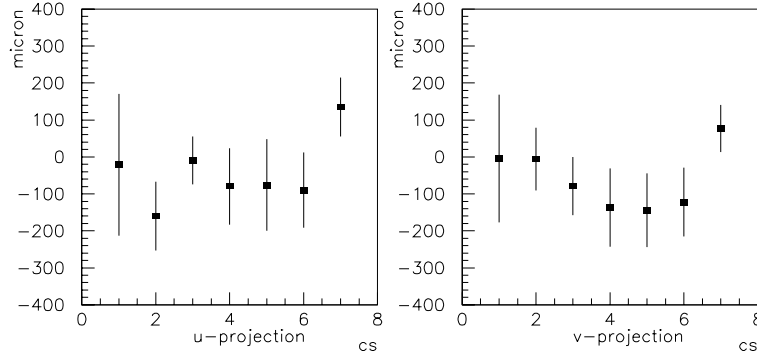


Fig. 6. Observed shift from the design between the emulsion and SFT coordinates.

calorimeter and muon identifier. The average neutrino energy was $53GeV$. Details of the prompt neutrino beam and the DONUT detector other than the emulsion targets are described in another paper (9).

The physics data was taken from April to September 1997. The effective total number of protons-on-target was 3.5×10^{17} . Because of high backgrounds from muons, neutrons and γ rays from the dump, all the emulsion modules were replaced once in to insure the recorded backgrounds were at a tolerable level.

In Table 3, summary of the exposure for each module is listed. The calculated number neutrino events in our modules are ~ 1100 events. Reconstruction of the triggered events using the counter information yielded 754 events in the fiducial volume. (9)

After exposure, fiducial marks were printed on all of the emulsion plates and developed. A coarse coordinate alignment with an accuracy of $10\mu m$ was obtained by using these marks.

Module	Style	Mass [kg]	POT $\times 10^{16}$	Expected event
mod1	ECC200 \times 47	104	20.1	236
mod2	ECC800 \times 19+Bulk \times 38	70	25.8	202
mod3	ECC200 \times 47	104	9.8	115
mod4	ECC200 \times 2+ ECC800 \times 7 + Bulk \times 47	70	14.7	115
mod5	ECC800 \times 21+Bulk \times 30	71	15.5	124
mod7	ECC800 \times 20+Bulk \times 32	70	25.8	203
mod8	Bulk \times 87	60	15.5	105
TOT				1100

Table 1

Information about the exposed emulsion modules.

4 Neutrino event location

4.1 Vertex prediction and Emulsion read-out

Using the information from the SFT, the reconstructed events were divided into three categories. Category (1): Only less than three tracks are emitted from the vertex. An example is shown in Fig.7. Category (2): At least three tracks are emitted from the vertex and the vertex position can be predicted within the accuracy of $10mm \times 10mm$ (Fig.8). Category (3): The vertex position is hard to be predicted within the accuracy of $10mm \times 10mm$ (Fig.9). The number of events belonging to each category is 138, 533 and 83, respectively.

The vertex location of category (1) events is not so easy as expected because of the high density background tracks accumulated during the run. So it is suspended. Also category (3), because of the limited scanning power at present, it is not so effective, so suspended.

For the events belonging to category (2), a prediction was made for the vertex position for each event, along with its calculated errors. This prediction determined the location and size of the scanning volume in an emulsion target.

Emulsion plates contained in the predicted volume were read-out by the present-generation automatic scanning system, the Ultra Track Selector (UTS). The typical scanning volume was $5\text{mm} \times 5\text{mm}$ perpendicular to the beam and $\sim 1.5\text{cm}$ along the beam. For the ECC(200) modules, about 12 plates were read-out. For each plate, both emulsion layers of a emulsion plate were digitized. For each bulk plate, only $\sim 100\mu\text{m}$ of the $350\mu\text{m}$ emulsion layer in the upstream-side was read-out.

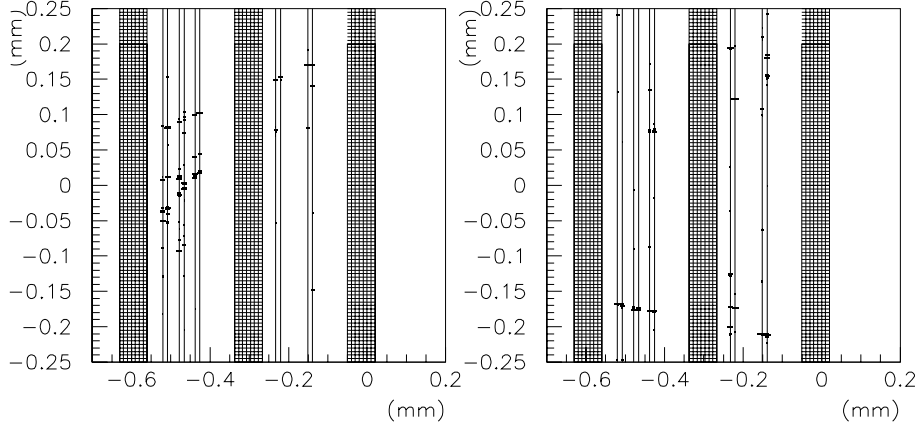


Fig. 7. A recorded neutrino event of Category (1).

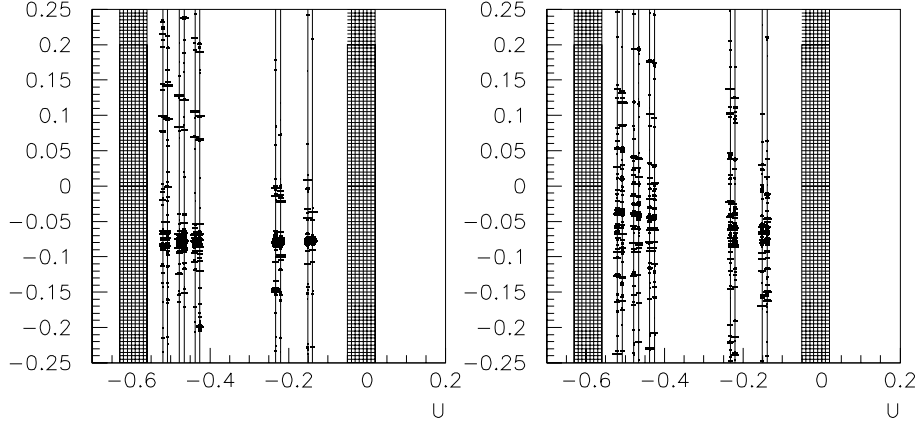


Fig. 8. A recorded neutrino event of Category (2).

The Ultra Track Selector(UTS) system is composed of a microscope installed on a computer controlled X-Y-Z stage, a CCD TV camera for image read-out, and a dedicated hardware processor to handle with the digitized tomographic images. Sixteen digitized images are taken by changing the focal position in an emulsion layer. Aligned grains across an emulsion layer were recognized as a track, which has reasonable hits in these sixteen digitized images. The output data from the UTS was the position, the angle and the pulse height of the

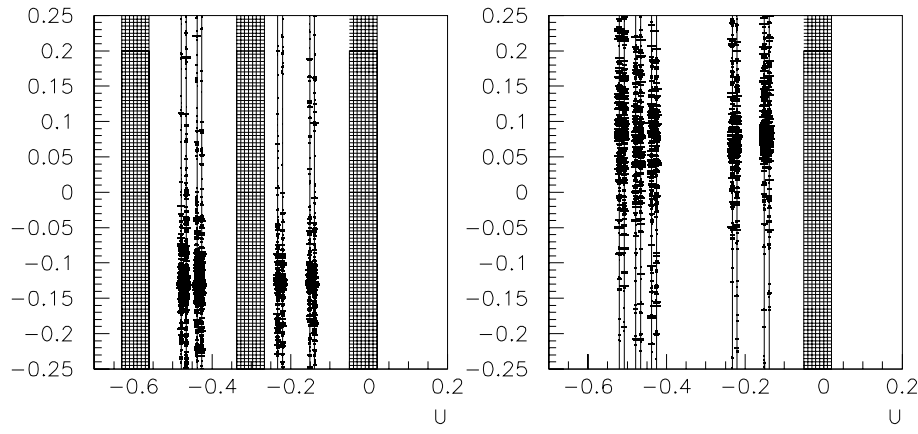


Fig. 9. A recorded neutrino event of Category (3). Note that each target station has a material corresponding to $2 \sim 3$ radiation lengths.

recognized tracks(called "micro-tracks"). Pulse height is the number of hits in the sixteen images. Track recognition is described in detail in Ref.(5; 6). For the UTS, the track angle was limited to be within 400 mrad perpendicular to the emulsion plate.

The read-out speed of the UTS corresponded to $\sim 1\text{cm}^2/\text{hour}$. For one plate ($5\text{mm} \times 5\text{mm}$ in area), ~ 15 minutes was required for the read-out. A single event needed about 6 hours for digitization, including plate changing.

Fig.10 shows an example of the recognized micro-tracks. There are about 800 micro-tracks in the displayed $1\text{mm} \times 1\text{mm}$ area. The origin of the micro-tracks includes not only the high energy muons or hadrons, which are interesting for event location, but also a background of low energy tracks arising from Compton scattering of gamma rays that were recognized as tracks by the UTS.

4.2 Track reconstruction and alignment

To reconstruct complete tracks in the event, a large number of background tracks recorded in the read-out volume were also reconstructed. These tracks were used to precisely align the emulsion layers.

The complete tracks were built layer-by-layer. Each track recognized in an emulsion layer was examined to see if it had a connectable micro-track in the adjacent emulsion layers. As shown in Fig. 11, the angle differences ($\Delta\theta$) between the micro-tracks and the connected-tracks (θ) and the position displacements (Δr) between the extrapolated positions were the parameters of the layer-by-layer alignment.

The essential tuning parameters were the distance between the emulsion layers

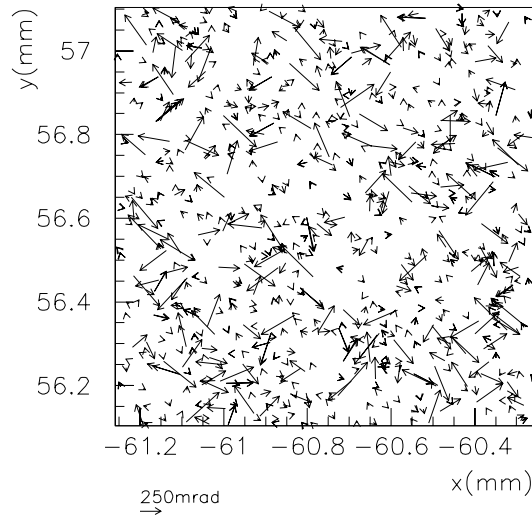


Fig. 10. A sample of the recognized tracks (micro-tracks) in one emulsion layer. The start of the arrow indicates the position of the micro-track and the length is proportional to the measured angle.

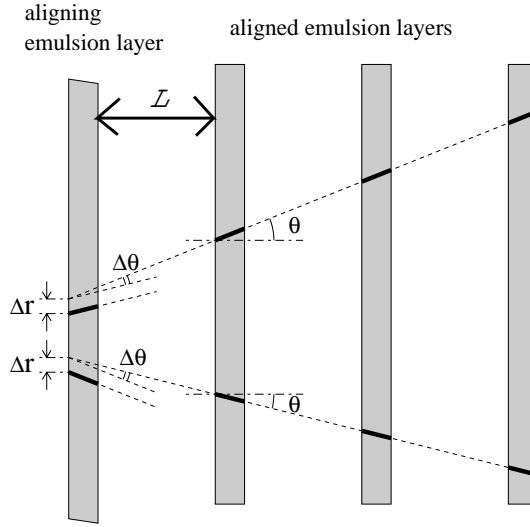


Fig. 11. The parameter definitions used for the track connection and the emulsion layer alignment.

(L), the relative shifts in transverse direction (X, Y) and the shrinkage of the emulsion layers. The measured $\Delta\theta$ was also affected by emulsion distortions. Because of these errors and the high track density, a micro-track can have multiple connectable micro-tracks within the spatial- and angular-tolerances, which were basically determined by the measured RMS of the distributions of $\Delta\theta$ and Δr .

For all tolerable combinations, angular difference and position displacement were calculated. The distribution of these parameters for the wrong combinations should be flat, while the distribution of correct combinations was peaked. Using the correct combinations from the peak, the position displacements and

angular shifts were calibrated. From the correlation between Δr and θ , the distances between layers were calibrated. And, from the correlation of $\Delta\theta$ and θ , shrinkage parameters of the emulsion layers were calibrated.

After these calibrations, the spatial and angular tolerance was reduced and micro-track connection was retried using the smaller tolerances. Repeating these corrections, RMS of $\Delta\theta$ and Δr are minimized and the number of correct combinations was maximized.

Fig.12 shows the distribution of the angle residuals ($\Delta\theta_x$ and $\Delta\theta_y$) and the position residuals (Δx and Δy) after the correction. After the corrections, a track was judged to be connected when $\Delta\theta \leq 3 \times \sigma_\theta + 0.05 \times \sqrt{\tan^2 \theta_x + \tan^2 \theta_y}$ and $\Delta r \leq 3 \times \sigma_r + 10\mu m \times \sqrt{\tan^2 \theta_x + \tan^2 \theta_y}$. Where σ_θ and σ_r are the RMS value of the residual distributions shown in Fig.12. These criteria filtered out the tracks with low momenta due to multiple scattering in the steel plates.

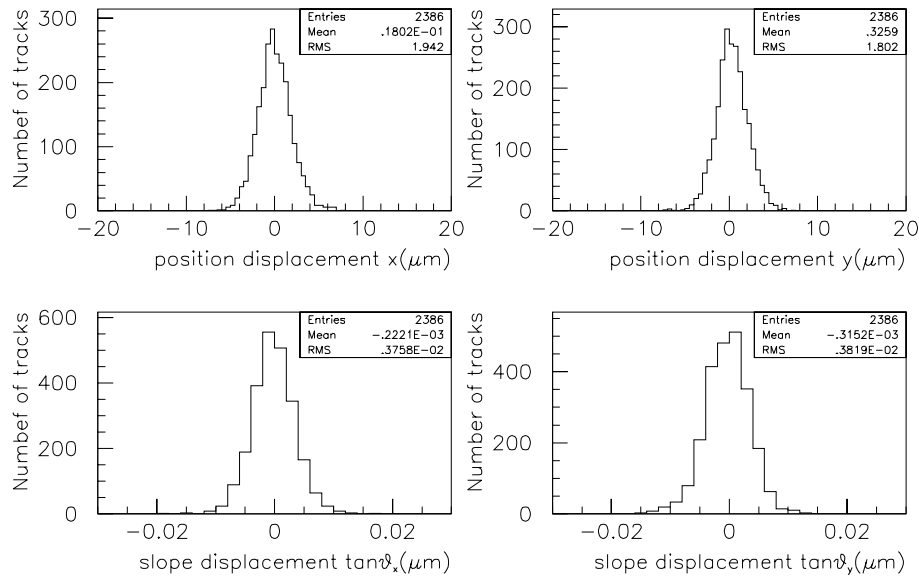


Fig. 12. Residual distributions of the position and the angle after the plate-by-plate connection.

Following the plate-by-plate connections, an additional "fine" alignment was tried by selecting relatively high momentum tracks, which were fully connected through the scanned volume. High momentum tracks were selected by comparing the angles in the upstream and the downstream of the scanning volume. The angles were reconstructed by using the first three or the last three micro-tracks at the upstream end or downstream end, respectively. The required angle difference was 2.4mrad for a track traversing 10mm of iron. This criteria corresponds to a constraint on the momentum $P \geq 9\text{GeV}/c$. After fine-tuning of the rotation and shrinkage of the plates, the measured position residuals were distributed as shown in Fig.13. The position residuals for each projection, i.e. position resolution of the plate, was $\sigma_{x,y} \sim 0.2\mu m$.

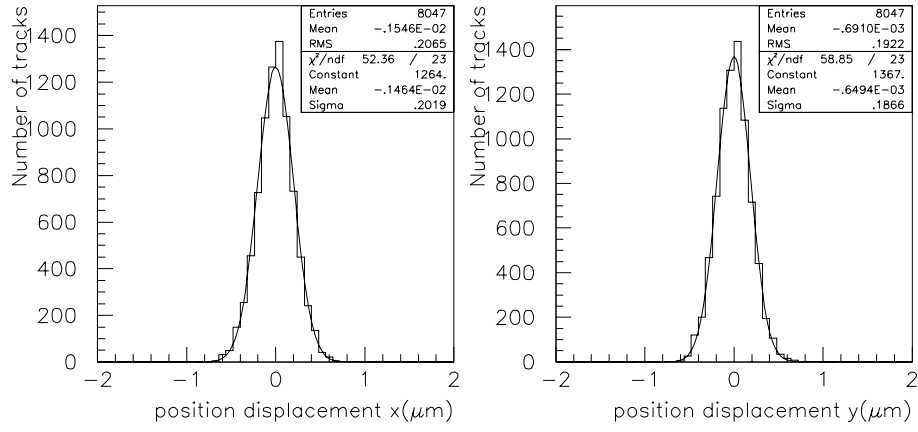


Fig. 13. Residual distribution for high momentum tracks after the plate-by-plate correction.

The position resolution of an emulsion plate was defined as $\sqrt{\sigma_x^2 + \sigma_y^2}$. Fig.14 shows the distribution of the measured resolution of emulsion plates for ECC(200), ECC(800) and Bulk type. The distributions have a peak at $0.3\mu\text{m}$ in the case of former two types and at $0.4\mu\text{m}$ in the case of Bulk plate. The distributions have tails over $1\mu\text{m}$. The origin of this degradation was investigated by using 79 examples which has the resolution greater than $1\mu\text{m}$ in any projection. It became clear that the origin of all of 79 is so-called a slipping of emulsion plates during the exposure.

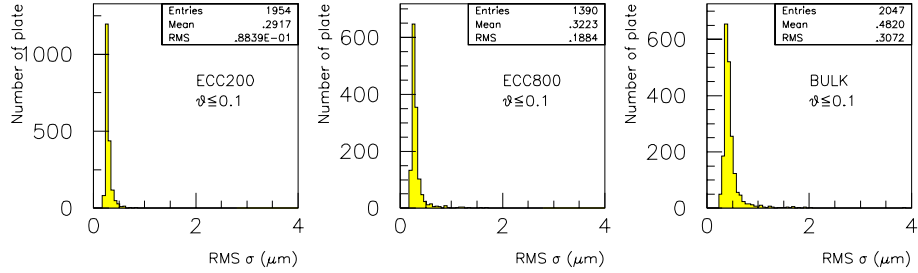


Fig. 14. Position *rms* distribution of (a)ECC(200), (b)ECC(800) and (c)Bulk plates.

The slipping was observed as the existence of multiple solutions of the plate-by-plate alignment. As shown in Fig.15, only one peak was observed in the case of no-slipping, but in the case of slipping the distribution has several peaks, which indicates that the relative position between plates was moved during the exposure. The origin of slip is considered to be the temperature variation during the exposure and the variation of the applied pressure.

Also, it became clear that the origin of the different size of the resolution between ECC and Bulk plates is so-called a local distortion. ECC and Bulk plates, which have typical resolution around the peak position of the distribution, were investigated. The distortion was observed as the angle difference between the recognized micro-tracks and the connected tracks across the base. As shown in Fig.16, the size of the distortion is larger in the case of Bulk plate.

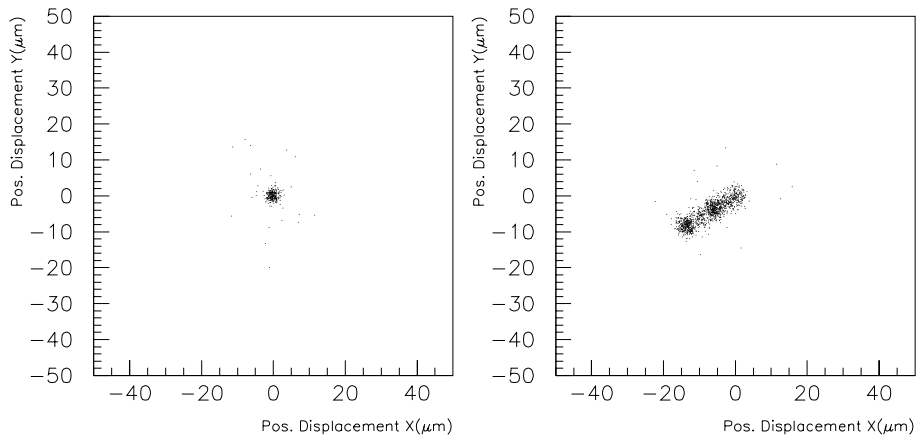


Fig. 15. Residual distribution for high momentum tracks after the plate-by-plate correction. (a) in the case of no slipping, (b) in the case of slipping

The origin of the distortion is the accumulated stress during the plate production; swelling and shrinking of the emulsion layer. Bulk plate has thicker emulsion layer and the size of the swelling and shrinking is larger than the ECC plates, which has thinner emulsion layer. This may contribute to the larger distortion in the Bulk plate.

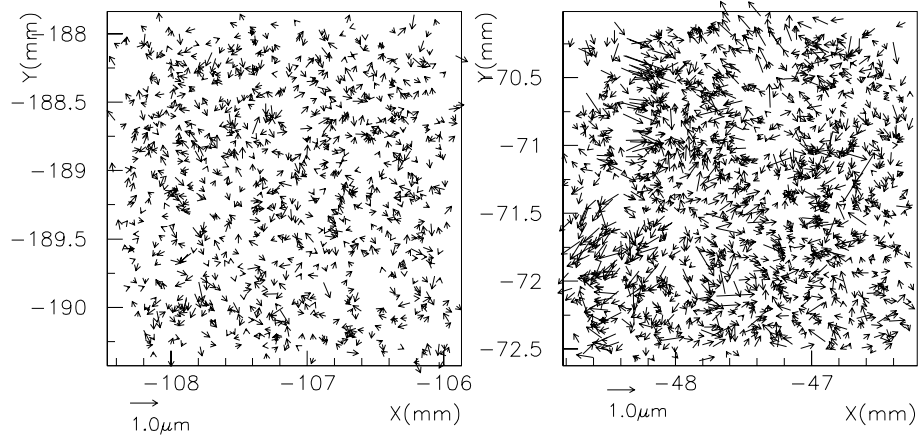


Fig. 16. Observed distortions, (a) in the case of ECC(200) and (b) in the case of Bulk plate

The track detection efficiency for each emulsion plate was also computed by checking for the existence of hits in all the emulsion layers along the penetrating reconstructed tracks. Fig.17 shows the distribution of the measured efficiency for each emulsion plate. The efficiency is lower in the case of ECC plates than the case of Bulk plates.

The origin of the inefficiency was investigated by checking the data quality of the emulsion plates with the efficiency less than 90%. Number of low efficiency data set are 10 among 2047 in the case of Bulk and 26 among 1910 in the case of ECC. Among the 10 data sets of Bulk plates, eight has dirty emulsion surface or quite large local distortion. On the other hand, in the case of 26

]

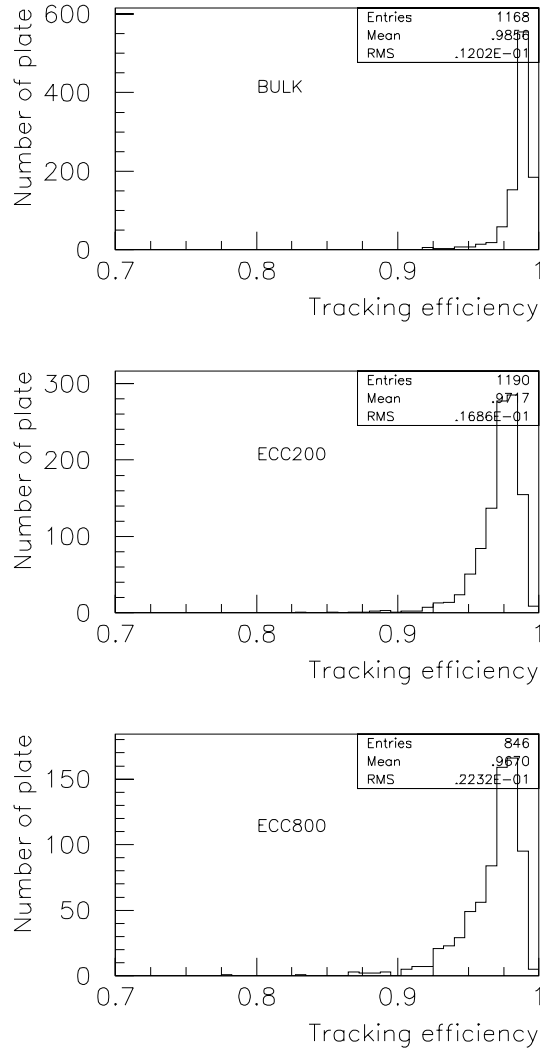


Fig. 17. Track detection efficiency of the emulsion plates. Inefficiency was due mainly to degraded emulsion quality such as a dirty surface, and large distortions.

data sets of ECC, only 8 have dirty emulsion surface or quite large distortions. Among the remained 18, 15 have low pulse height of the recognized tracks. The origin of this low pulse height is in thin emulsion layers or low grain densities. As the emulsion plates for DONUT were the hand-made one, quality control was limited regrettably. The over all efficiency for detecting micro-tracks was measured to be over 97%.

4.3 Vertex location

4.3.1 Procedure

In order to select the tracks from a neutrino interaction vertex and reject the background muons the scanning volume, the following criteria were applied sequentially: (1) Tracks must have started within the volume and have no connectable micro-tracks in the two adjacent upstream emulsion layers. This requirement rejects the penetrating tracks efficiently. (2) Tracks must be constructed from at least three micro-tracks. (3) The χ^2/ndf ($ndf = 8$) defined by the first three micro-tracks must be smaller than 2.5. Cuts (2) and (3) greatly reduced tracks of low momenta.

Fig:18(a) illustrates the effect of the above cuts on the emulsion data after alignment. A large number of tracks were typically reconstructed in the scanning volume. The tracks are mostly penetrating muons originating from the dump. The muon track density depends on the somewhat on target position, and in the figure it is about 12000 tracks in $/ 5mm \times 5mm$. The tracks from the neutrino interaction were isolated in this sea of background tracks. The next plot in the sequence, Fig.18(b), shows the same data after cuts (2) and (3), with 264 tracks remaining.

Next, (4) the remaining tracks were tested for vertex topology. At least three tracks were required to be associated such that all impact parameters at the best vertex position were less than $4\mu m$.

After the vertex requirements were imposed, only a few vertex candidates remained. To confirm a vertex candidate, (i) the emulsion plates near the vertex point were investigated using a manually controlled microscope and (ii) the emulsion track information was compared with the hits in the SFT.

By the manual check (i), the candidate A and B were identified as fake vertexes. In the case of A, two tracks were created the vertex. But these two tracks have penetrated to the upstream. This was caused by the inefficiency of the UTS and misconnections of the offline processes. In the case of B, two tracks, which created the vertex, were low momentum tracks and were not connected to upstream because of large multiple scattering. Candidate C and D were the real vertexes. D has two tracks with small relative angle, which is consistent with an electron pair creation. C has seven tracks as shown in Fig.18(c). After applying the vertex constraint (ii), candidate C was selected.

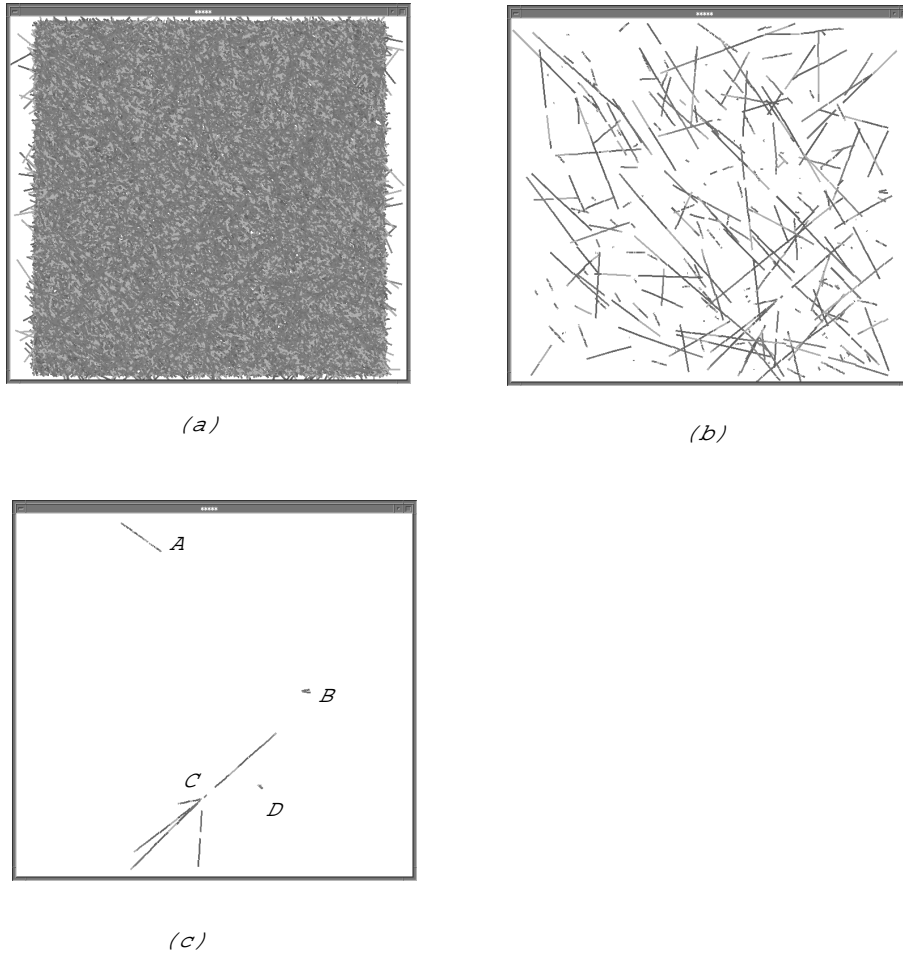


Fig. 18. Vertex location sequence by the NETSCAN in the case of a event (Run3118event11989). (a)After alignment, (b)after the rejection of penetrating tracks, (c)after the vertex requirement.

4.3.2 Efficiency

By December 2001, vertex location was attempted for category (2) 533 events and 337 events were confirmed as being located.

The reason of the failure of the vertex location was investigated. At first the data set quality was checked. As described above, the data quality is corresponding to the plate quality contained in the data sample. Dependences of the vertex location efficiency on the position resolution of the plate and on the track detection efficiency of the plate were checked.

Fig.19 and Fig.20 show the vertex location efficiency dependence on the resolution of the worst quality plate contained in the data set and on the track detection efficiency of the worst quality plate. The event location efficiency gradually decreases when the plate quality becomes worse.

]

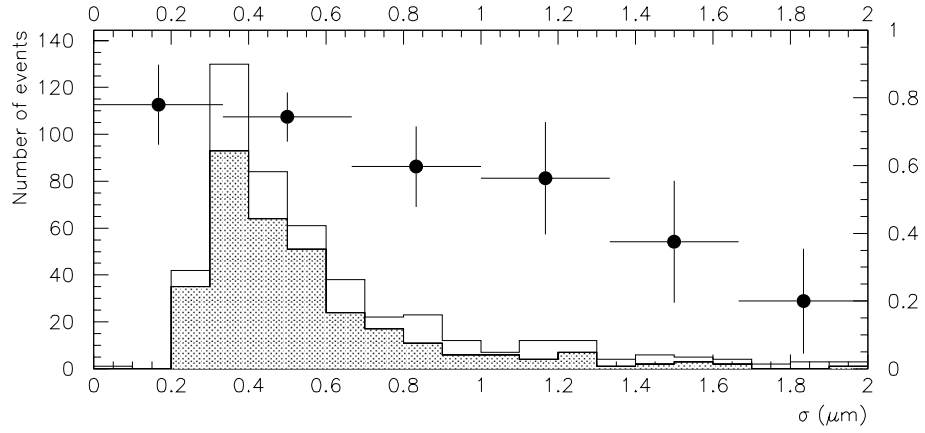


Fig. 19. Dependence of the vertex location efficiency on the position resolution of the worst quality plate among the data set.

]

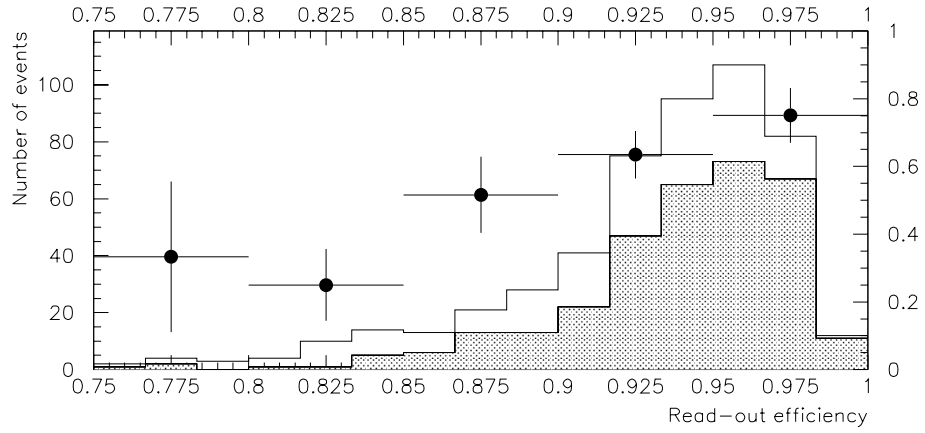


Fig. 20. Dependence of the vertex location efficiency on the track detection efficiency of the worst quality plate among the data set.

Table.4.3.2 shows the categorization of the event quality and Table.4.3.2 shows the vertex location efficiency of each category. For the good quality samples, the location efficiency reach to $\sim 76\%$.

There are small differences between ECC200, ECC800 and Bulk, even in the good quality samples. The location efficiency is 69%, 73% and 84%, respectively. For these good quality samples, the location efficiency dependence on the depth (radiation lengths) was checked. Fig.21 shows the result for each target type. Generally, it was more difficult to locate events in the upstream part of the emulsion target, which is readily seen for the ECC(200) type. Clearly, one reason why the upstream location efficiency was poor was the reduced accuracy of the vertex prediction. Therefore to increase the efficiency, the scanning volume could be enlarged, but this would require a more powerful scanning system. The next-generation emulsion read-out system, called "S-UTS", is under development in order to meet such increased demands. (10).

Plate Type	Number of events	Good quality $\sigma^{worst} \leq 1.0\mu m$ & $\epsilon^{worst} \geq 0.9$	Bad quality $\sigma^{worst} \geq 1.0\mu m$ or $\epsilon^{worst} < 0.9$
ECC(200)	152	115	37
ECC(800)	174	91	83
Bulk	208	132	76
Total	533	338	195

Table 2
Quality of the NETSCAN data

Plate Type	Good quality		Bad quality	
	Tried event	Found event (Location efficiency)	Tried event	Found event (Location efficiency)
ECC(200)	115	79(69%)	38	21(55%)
ECC(800)	91	67(73%)	84	21(25%)
Bulk	132	111(84%)	80	38(48%)
Total	338	257(76%)	195	80(41%)

Table 3
Dependence of the vertex location efficiency on the data set quality.

5 The Decay Search

5.1 Decay Search Volume

For the located events, a smaller volume around the located vertex was digitized again in order to optimize scanning acceptance and precision for detecting tau decays. The scanning volume was $2.6mm \times 2.6mm$ and the length was nominally $1.2cm$. The same track reconstruction procedure used for the vertex location was also applied for the new data, to confirm the vertex. The tau decay search was divided into two categories by the topology, as shown in Fig.22: long flight decay search and short flight decay search. In the first case, both the parent and the daughter tracks were present in the emulsion data. In the second, only the daughter could have been detected.

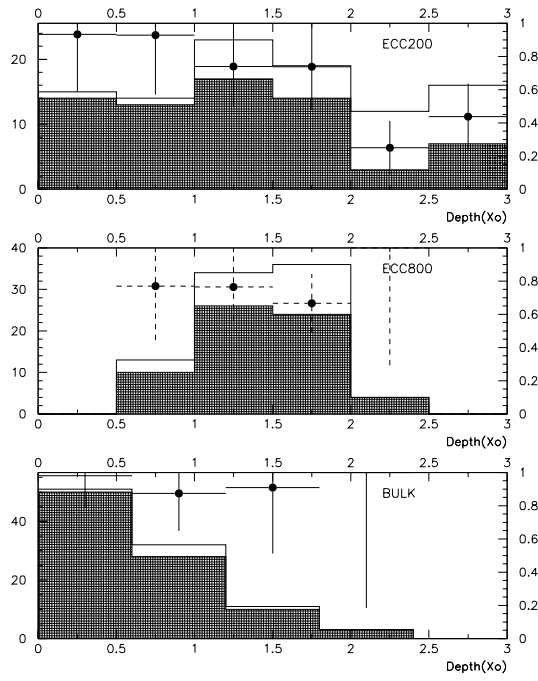


Fig. 21. Dependence of the vertex location efficiency on the vertex depth from the SFT (neutrinos come from the right). Solid-line histogram: number of predictions, filled histogram: number of found events. The open circles indicate the ratio of number of found events to the predicted number (scale on the right).

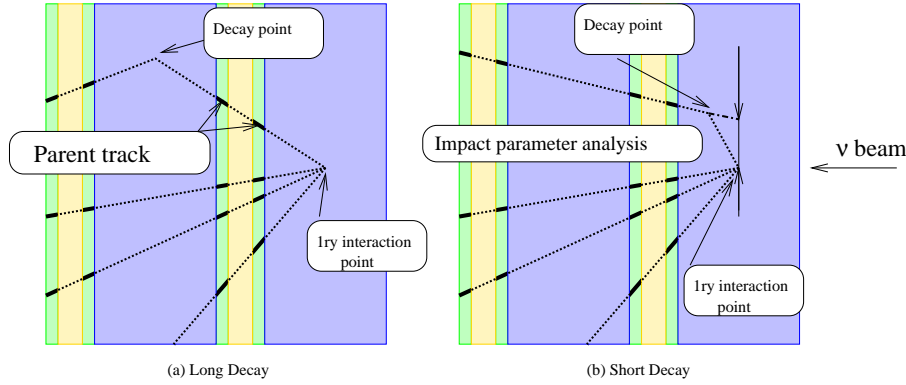


Fig. 22. Decay search topology was divided into two categories: (a) Long flight decay search where the parent tau *and* the daughter can be observed, and (b) Short flight decay search where only the daughter particle can be detected by a non-zero impact parameter to the vertex.

5.2 Topological decay search : Long Flight Decay

A general search for long lived decays of tau lepton and charm mesons began by trying to link tracks from the interaction vertex with all other tracks defined by the following criteria: (1) the track must start downstream of the vertex and, (2) the tracks were composed of at least three micro-tracks and, (3) the

fitted χ^2/ndf of the first three micro-tracks should be smaller than 2.5 and, (4) the distance of closest approach between the parent candidate and the daughter was smaller than $5\mu m$.

With these cuts, 37 events (48 tracks) were selected. Fig.23 shows the angle distribution between the parent track and the daughter.

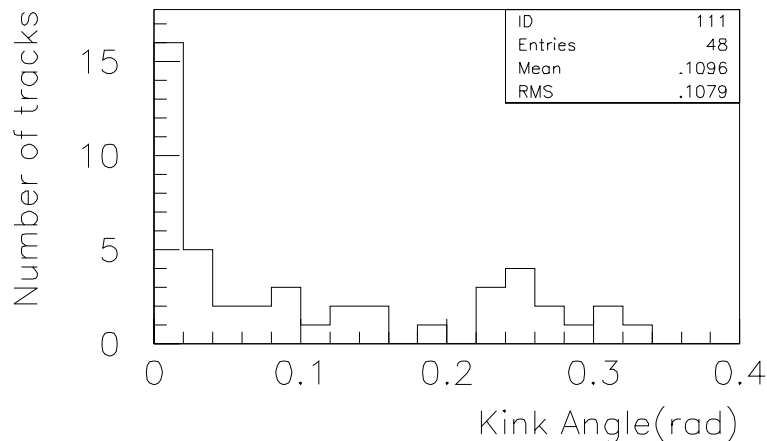


Fig. 23. Kink angle distribution of the detected long flight decay candidates.

The above selection may have failed, however, for decays with an angle between the parent and daughter of less than 15 mrad. For these there was a possibility that the parent and the daughter were coalesced into one track, where the track was assembled from the micro-tracks. This possibility was checked for all of the tracks from the vertex using the following procedure.

Each track from the vertex, which was composed of micro tracks, was divided into two tracks, refit and the angle difference between them was computed, and then repeated, by changing the dividing point as shown in Fig.24. If the angular difference was larger than 5mrad it was picked up and investigated further. The detection efficiency has a dependence on the position where the decay occurs. The expected sensitivity to the kink angle is shown in Fig.25, which was estimated by using penetrating muons through 10 plates. The sensitivity was estimated at $1.7mrad$ which is defined as $3 \times \sigma_{measured}$, except for the edge layers ($5 \sim 6mrad$).

The following additional cuts were applied to the 1549 tracks in 344 events found with small kink angles: (1) $\theta_{meas} \geq 3 \times \sigma_{meas}$, (2) the parent segment must contain at least three micro-tracks. (3) The daughter segment must have at least three micro-tracks. (4) The impact parameter to the vertex of the daughter track is greater than $5\mu m$. After these cuts 117 tracks remained, with the distribution of their detected kink angle shown in Fig.26.

The tau and charm physics long decay sample had three additional requirements: (1) the topology was limited to one prong or three prongs decay, and

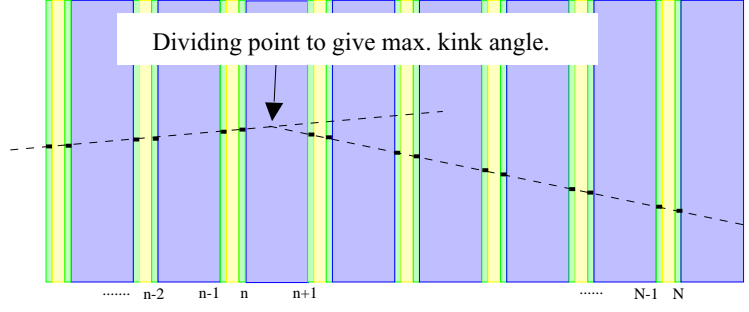


Fig. 24. Schematic view of the small angle kink detection. A track was split into two tracks at a reference point and the "kink angle" was determined for the series of reference points.

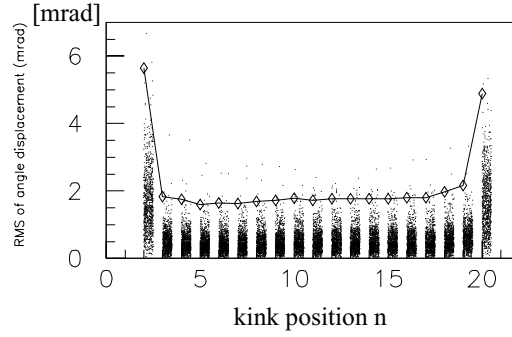


Fig. 25. The sensitivity to small kinks in the study illustrated in reffig:LSearch.

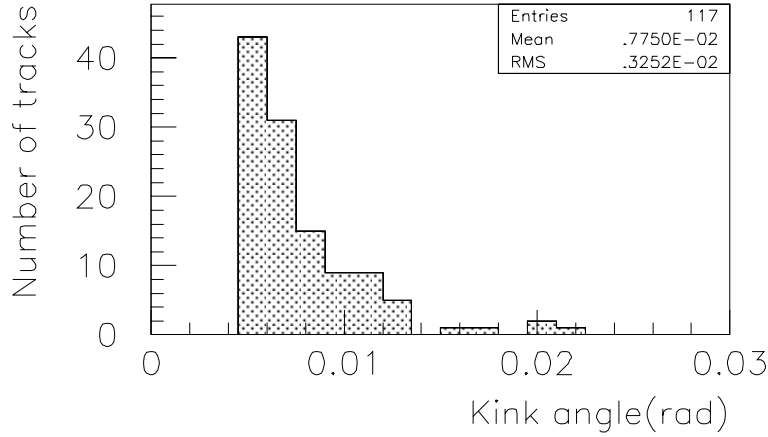


Fig. 26. Detected kink angle distribution in the small kink search.

(2) the impact parameter of the daughter particle to the primary vertex was less than $500\mu m$, and (3) $(\theta_{kink} = |\theta_{daughter} - \theta_{parent}| \geq (\theta_{parent} - 0.1)/2)$. Both (2) and (3) were incorporated to reduce the number of low-energy interactions, with a negligible effect on tau decay efficiency.

Sixty-four tracks in 60 events were selected from 37+117 long flight decay candidates. The distribution of the detected angle is shown in Fig.27.

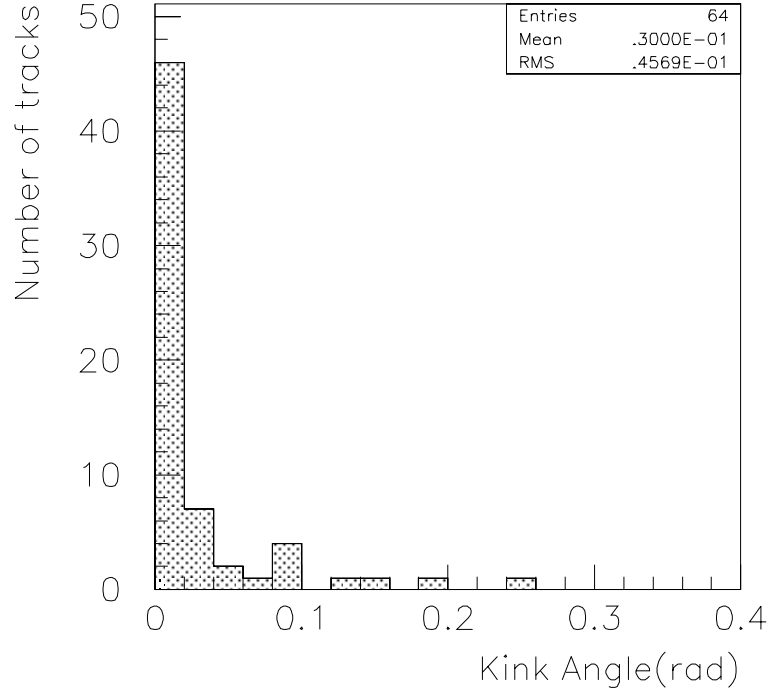


Fig. 27. Angle distribution between the parent track and the daughter (long flight decay search).

5.3 Topological decay search : Short Flight Decay

The short-flight decay search required the following criteria. (1) The track started at one or two emulsion layer downstream from the located vertex. (2) The impact parameter to the vertex is less than $200\mu m$. (3) The track is composed by at least three micro-tracks. (4) the distance of closest approach between

Closest approach between the selected two tracks is calculated. The signal is pre-selected by applying the cut on the minimum distance (MD) of the pair. The criteria is $MD > 1.36 + 1.36 \times 10^{-3} \times dZ\mu m$, $MD > 1.52 + 1.02 \times 10^{-3} \times dZ\mu m$ and $MD > 2.04 + 1.81 \times 10^{-3} \times dZ\mu m$ in the case of ECC(200), ECC(800) and Bulk, respectively. Where dZ is the distance from the most upstream emulsion layer and the position where the closest approach occurs. This cut was calculated from the measurement error, which was obtained during the alignment. 78 events were selected for further investigation.

6 Decay Analysis

Candidates selected by the above procedures may contain tau decays, charm decays, secondary interactions and scattering of low energy particles. To resolve these hypotheses, the momentum of the daughter tracks was measured and the decay Pt computed, and all tracks in the event (including the daughter) were checked to see if any is consistent with being a lepton (muon or electron) using the spectrometer.

6.1 Momentum measurement by multiple Coulomb scattering measurement

Although DONUT had a magnetic spectrometer, the efficiency for unambiguously linking SFT tracks with drift chamber information was low because of electromagnetic shower development in the thick emulsion targets.

An alternative momentum estimate was to use multiple Coulomb scattering (MCS) in the emulsion data. The emulsion data was not significantly affected by confusion in tracking, and, in principle, momentum estimates were available to all the tracks in an event. A schematic overview of the principle of the MCS method is shown in Fig.28.

The root mean square of the position displacement in one projection (y) is expressed as $y_{RMS} \equiv \sqrt{\langle y^2 \rangle} = \sqrt{2/3} \times k/p\beta \times \sqrt{t/X_0} \times t$, where k is the scattering constant, p and β is the momentum and the speed of the track, t is the thickness of the material and X_0 is the radiation length of the material. The expected value of y_{RMS} is $4.0\mu m$ in the case of $1GeV/c$ particle and the ECC with 1mm thick Iron plate. This value can be compared with the extrapolation error from the base track ($1.5\mu m \sim \sqrt{1 + ((L1 + L2)/L1)^2 + (L2/L1)^2} \times \text{resolution}$ ($\sim 0.2\mu m$), where $L1$ is the length of the base line ($200\mu m$) and $L2$ is the extrapolation length ($1mm$) in the case of ECC200).

The y_{RMS} has $t^{3/2}$ dependence from MCS, but the measurement error is independent of t . This dependence allowed the measurement of higher momentum particles by increasing t so that the displacement was observable. It should be noticed that a good plate-by-plate alignment by NETSCAN procedure was indispensable for this measurement.

The measured y_{RMS} (y_{RMS}^{meas}) was the addition of the y_{RMS} from MCS and the measurement error: ϵ_y . $y_{RMS}^{meas} = \sqrt{y_{RMS}^2 + \epsilon_y^2}$. Since ϵ_y was measured in the alignment sequences as described in the previous section, one could estimate the y_{RMS} confidently.

The distribution of y was described by a Gaussian distribution to a good approximation. The momentum of a track was extracted from the measured standard deviation, with the accuracy $\Delta(y_{RMS})/y_{RMS}$ expressed as $1/\sqrt{2n}$, where n was the number of independent measurements. If 11 independent position measurements were used, giving 10 displacements, the error was 22% in principle.

[Coordinate Method]

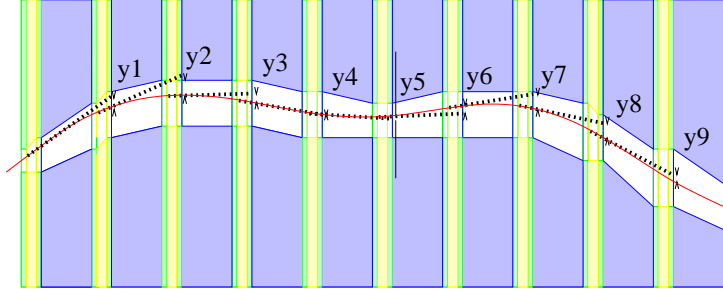


Fig. 28. Schematic figure of the momentum measurement by using the information of multiple Coulomb scattering. In the emulsion plates, the track path was measured with sub-micron accuracy.

6.1.1 Check 1: Test experiment

In order to check the validity of this method, an ECC-type stack with 29 bulk emulsion plates was exposed to a $4\text{GeV}/c$ π^- beam at KEK. Fig.29 shows the result of the dependence of the y_{RMS}^{meas} on the t . Here y_{RMS}^{meas} is the average over 384 tracks reconstructed in the chamber. The fit value is $y_{RMS}(t) = \sqrt{(94.49(t/Xo)^{3/2} + 1.458^2)}$. This result is consistent with the measurement error. The scattering constant k was determined to be $16.02\text{MeV}/c$. The distribution of the MCS estimated momentum for each track is shown in Fig.30. The resolution of the momentum measurement was about 30%.

6.1.2 Check 2: Spectrometer tracks

One can also check the MCS measurements with momenta estimated using the magnetic spectrometer. Care was used in selecting tracks that were well-reconstructed and had no evidence of interaction in the target area. For these tracks, the momentum was estimated by the MCS method. The scatter plot between the MCS measured and spectrometer measured momentum is shown in Fig.31. The correlation is strong up to $20\text{GeV}/c$.

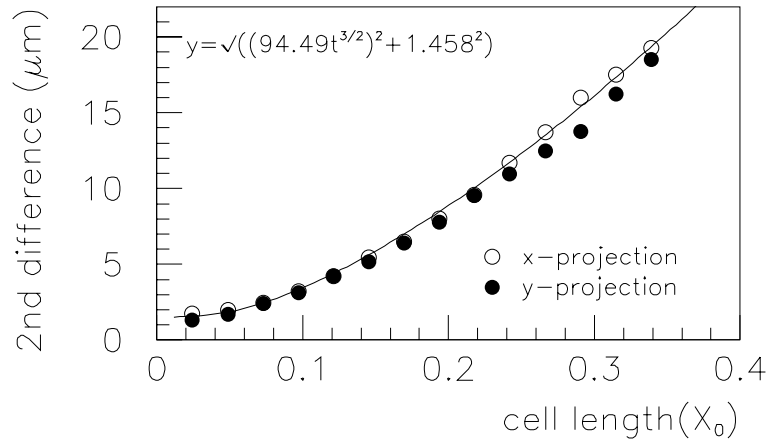


Fig. 29. Dependence of the position displacement on the cell length or thickness. Open circles : x projection, and solid circles: y projection. The fit is shown by the curve.

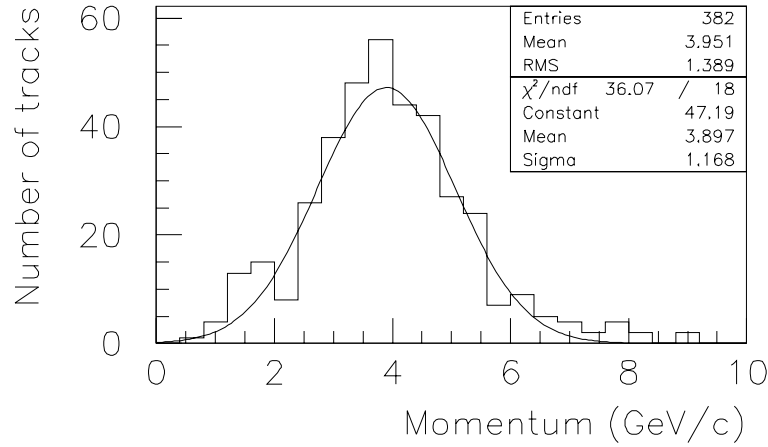


Fig. 30. Measured momentum distribution of $4\text{GeV}/c$ π^- tracks.

6.1.3 Check 3: Momentum of the secondary particles

Using 942 secondary tracks from 269 located events (a subset of the 344 events), the MCS momenta were computed and the resulting distribution was compared with a Monte Carlo distribution. The results are shown in Fig.32. The MCS momentum estimate provided a way to estimate the total event energy, which could only have been done for a few events using the magnetic spectrometer.

6.1.4 Analysis of the Candidates

The momenta of the daughter tracks of the found candidates were measured by the MCS method. The resulting Pt distribution of the long flight decay candidates with kink topology is shown in Fig.33.

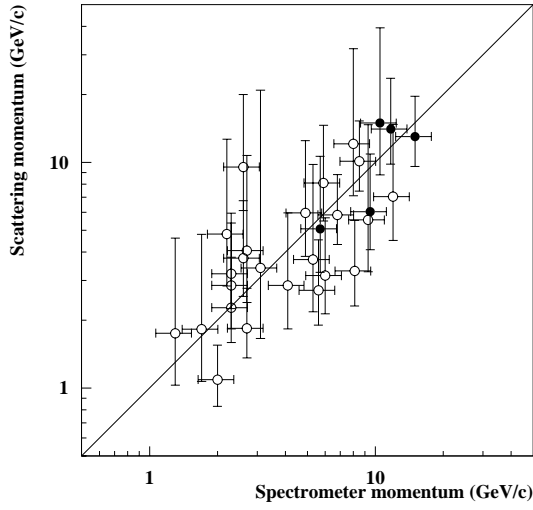


Fig. 31. Correlation between the momentum measured by the MCS method and by the magnetic spectrometer. Filled circles indicate identified muons.

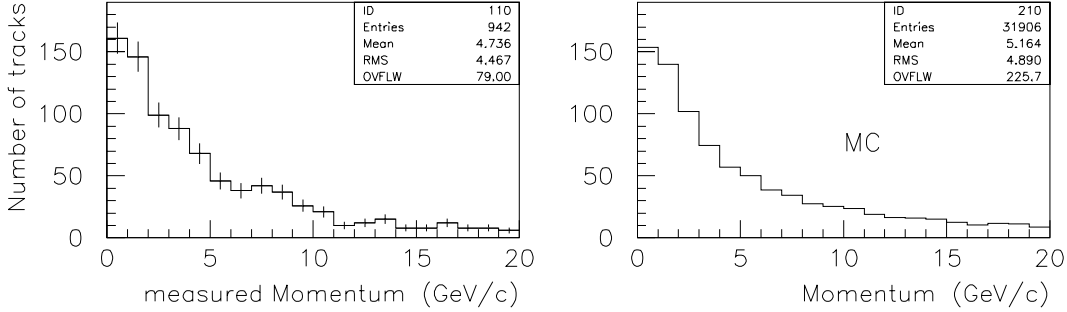


Fig. 32. Momentum distribution of the secondary particles, (a) measured by the MCS method. (b) Monte Carlo expectation. The scale of figure (b) is normalized to (a).

For the short flight decay candidates, the measured impact parameter (MD) was investigated to see if it was consistent with the displacement due to multiple Coulomb scattering determined by the measured momentum of tracks. If the measured impact parameter was at least four times larger than the expected error, a parameter, Pt_{min} , was calculated. The transverse momenta of short decays cannot be determined since the decay is only constrained to a line in space and not a point. Pt_{min} was defined as the MCS momentum of the daughter times the decay angle assuming that the decay occurs at the downstream edge of the steel plate in which the vertex was located (note that the short decay analysis applies only to ECC-type targets). The Pt_{min} distribution of the 11 short decay candidates is shown in Fig.34.

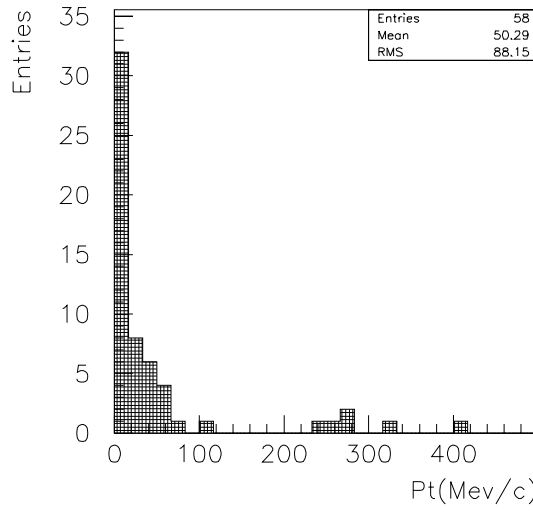


Fig. 33. Pt distribution of the detected long flight decay candidates.

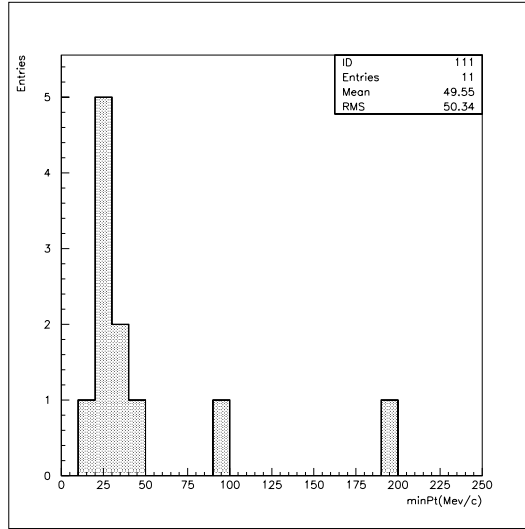


Fig. 34. Pt_{min} distribution of the detected short flight decay candidates.

6.2 Electron identification by cascade shower detection

In order to discriminate tau decays from charm decays that were associated with charged current interactions of $\nu_e, \nu_\mu, \bar{\nu}_e$ and $\bar{\nu}_\mu$, the existence of a lepton(s) from the interaction vertex was checked.

Muons were identified conventionally with proportional tube hodoscopes downstream of steel walls. The acceptance was estimated to be 70% by a Monte Carlo. Details regarding lepton identification with the spectrometer can be found elsewhere []. The identification of electrons from the primary interaction was done in the emulsion targets themselves, for most events. In the emulsion, the start of an electromagnetic cascade shower was clearly identified. Another indicator is the rapid energy loss by the bremsstrahlung, which appeared as

an increase of the position displacement or of the angle alternation by multiple Coulomb scattering as described above. The identification efficiency has a dependence on the track length followed in the emulsion. Fig. 35 shows the estimated electron identification efficiency for the electrons comes from the ν_e^{cc} . If the track can be followed for at least two X_o , it approaches 85%. Fig. 36 shows one kink event identified as charm production in ν_e^{cc} .

The same identification process can be applied to the daughter track candidates. Two events in the analysis sample had daughter electrons that were identified in the emulsion, and since no other electron, or muon, was found coming from the neutrino interaction, both events were identified as likely ν_τ interactions.

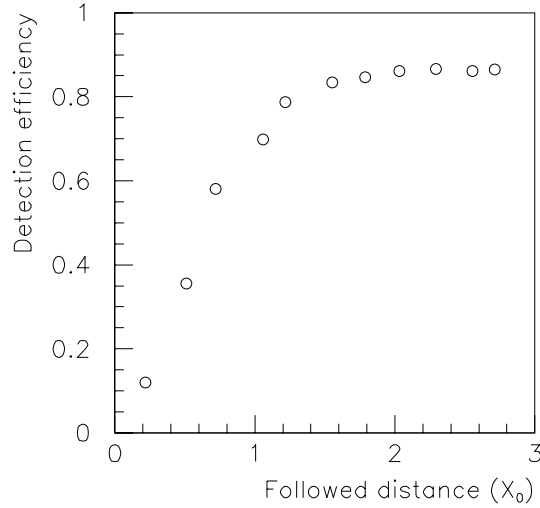


Fig. 35. The ν_e^{CC} identification efficiency as a function of the track length.

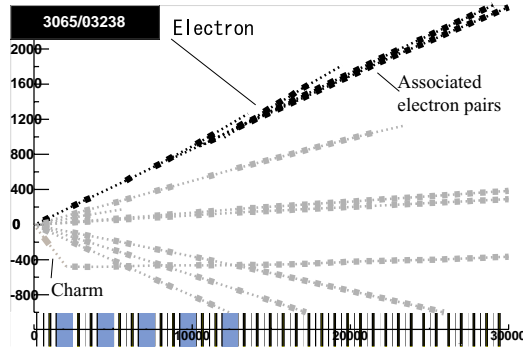


Fig. 36. Identified charm event produced in a ν_e^{CC} . The upper track was identified as an electron by finding the associated electron pairs. The charm decayed into one track, shown in the figure near the bottom.

6.3 Detection Efficiency of Tau Decays

The detection efficiencies of τ^- from ν_τ^{CC} and τ^+ from $\bar{\nu}_\tau^{CC}$ were estimated by Monte Carlo, which included the measured tracking efficiencies and the resolutions of the emulsion plates. Fig.37 shows the dependence of the τ decay detection efficiency on the Pt and Pt_{min} cut for the long and short flight decay search. The short flight to long flight ratio is significantly different between the ν_τ^{CC} and $\bar{\nu}_\tau^{CC}$ interactions.

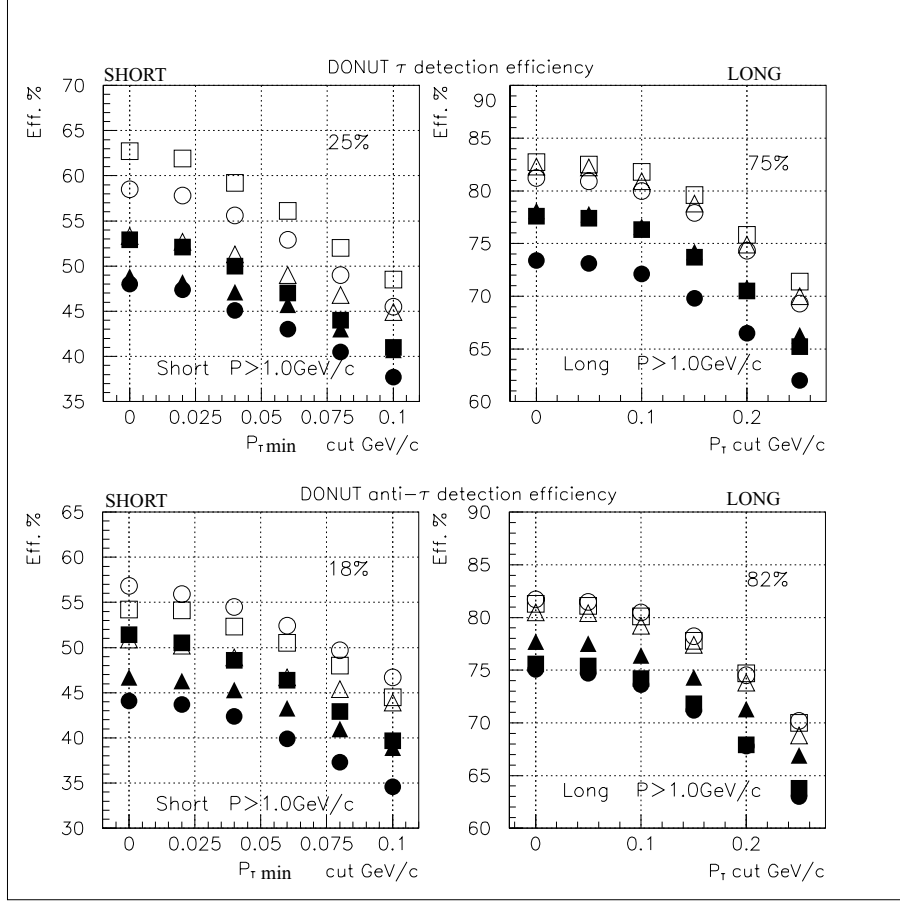


Fig. 37. Dependence of the tau decay detection efficiency on the Pt and Pt_{min} cut for the case of long and short flight decays. Top: τ^- from ν_τ^{CC} . Bottom: τ^+ from $\bar{\nu}_\tau^{CC}$. Right: Long flight decay. Left: Short flight decay. The squares, circles and triangles show the results for ECC200, ECC800 and Bulk, respectively. Open symbols indicate perfect micro-track detection efficiency and the filled symbols show the results for measured plate efficiencies.

7 Summary

The NETSCAN method of digitizing a large volume of emulsion data, devised for the DONUT analysis, was very effective for the vertex location and decay search. The NETSCAN data was also used successfully for more detailed event analysis, including momentum estimation and electron identification. The effectiveness of the NETSCAN analysis was largely due to the precise, sub-micron level of alignment achieved by careful calibration.

Those features can be considered as revivals of several capabilities of the original ECC. In 1971, the discovery of X-particles (charm particles) was achieved in the analysis of the ECC exposed to cosmic rays (11). Very precise decay search, momentum measurement by the MCS method and not only the identification but also the energy measurements of electromagnetic showers were performed in the analysis. But it required about three months to analyze one event, because it was performed under fully human operated microscopes. In contrast with this situation, in DONUT analysis, with the help of UTS system, about 4 events can be analyzed per day per UTS.

The ECC can be now be considered as a general-purpose detector. Even muon identification can be possible if a number of ECC modules can be aligned along the beam. Also it is possible to determine the sign of the charged particles by installing the ECC in a magnetic field. In DONUT, the downstream counters took these last two roles.

The research and development of advanced emulsion read-out systems is still in progress. With increasing scanning power, nuclear emulsion can have much wider applications in the field of elementary particle physics (especially in the neutrino physics), nuclear physics and general radiation measurement.

8 Acknowledgement

We would like to thank the support staffs of Nagoya University and the collaborating laboratories. We acknowledge the support from the Japan Society for the Promotion of Science, the Japan-US Cooperative Research Program for High Energy Physics, the Ministry of Education, Science and Culture of Japan, the U.S. Department of Energy, the General Secretariat of Research and Technology of Greece, the Korean Research Foundation, and the DOE/OJI Program.

References

- [1] K.Kodama et al., DONUT Collaboration, Phys. Lett. B504(2001)218-224.
- [2] N.Ushida et al., E531 collaboration, Nucl. Instr. And Meth. A224(1984)50-64.
- [3] Aoki S. et al., CERN WA75 Collaboration, Nucl. Instr. Meth. A274(1989) 64-78.
- [4] K.Kodama et al., Nucl. Instr. and Meth. B93(1994)340-354. K. Kodama et al., Nucl. Instr. And Meth. A289(1990)146-167.
- [5] S. Aoki et al., Nuclear Tracks 12(1986)249-252.
- [6] S. Aoki et al., Nucl. Instr. and Meth. B51(1990)466-472.
- [7] E.Eskut et al., CHORUS collaboration, Nucl. Instr. and Meth. A401(1997)7-44.
- [8] Nakamura M., Proceedings of SCIFI93, (1995)194-201. Nakano T. et al., Proceedings of SCIFI93, (1995)525-533. Nakano T. et al., IEEE on NS, NS39(1992)680-684.
- [9] K.Kodama et al., will be submitted to Nucl. Instr. and Meth.
- [10] Nakano T., Proceedings of International workshop of Nuclear Emulsion Techniques, 1998 NAGOYA.
- [11] K. Niu *et al.*, Prog. Theor. Phys. **46**(1971) 1644.